



Relating capillary pressure to interfacial areas

Laura J. Pyrak-Nolte,^{1,2} David D. Nolte,¹ Daiquan Chen,^{2,3} and Nicholas J. Giordano¹

Received 13 August 2007; revised 4 December 2007; accepted 22 January 2008; published 11 June 2008.

[1] Experiments were performed on transparent two-dimensional microfluidic porous systems to investigate the relationships among capillary pressure and the interfacial areas per volume between two fluid phases and one solid phase. Capillary pressures were calculated from the observed interfacial curvature of the wetting-nonwetting interface, and these correlated closely to externally measured values of applied pressure. For each applied pressure, the system established mechanical equilibrium characterized by stationary interfaces, uniform curvatures across the model, and random surface normals. To study the relationships among capillary pressure and the interfacial areas, we compare the curvature-based capillary pressure with the differential change in interfacial areas per volume as a function of wetting-phase saturation. The differential pressure contributions calculated from the experimental measurements are found to be nearly independent of the measured capillary pressure. These results suggest that other contributions to the capillary pressure must be significant when imbibition and drainage processes result in saturation gradients.

Citation: Pyrak-Nolte, L. J., D. D. Nolte, D. Chen, and N. J. Giordano (2008), Relating capillary pressure to interfacial areas, *Water Resour. Res.*, 44, W06408, doi:10.1029/2007WR006434.

1. Introduction

[2] The distribution of two immiscible fluid phases in a porous medium is predicated on the Young-Laplace equation which relates capillary pressure, p_c , to the geometry of the fluid-fluid interface through the interfacial tension between the two immiscible fluid phases

$$p_c = \gamma^{wn} \left(\frac{1}{R_1} + \frac{1}{R_2} \right) = \gamma^{wn} K \quad (1)$$

where γ^{wn} is the interfacial tension (also referred to as surface tension) between the wetting, w , and nonwetting, n , phases and K is the mean curvature of the interfaces based on the principal radii of curvature of the surface, R_1 and R_2 . The cohesive and adhesive forces among the fluid phases and the solid are determined by whether a fluid is a wetting phase or a nonwetting phase. The equilibrium contact angle is defined as the angle between the solid surface and the tangent to the liquid surface at the line of contact with the solid [Barnes and Gentle, 2005]. A wetting-phase fluid exhibits a contact angle that is less than 90° and tends to spread out and wet the solid. When two immiscible fluids are present, one fluid wets the surface, tending to displace the other fluid from the surface. In equilibrium, the forces among the fluids and the solid are balanced and produce a curved interface between the two fluid phases. A curved

interface between two fluids indicates that a pressure difference exists across the interface, and this pressure difference is balanced by the surface tension forces. This pressure difference is referred to as the capillary pressure. At equilibrium, p_{ceq} is defined by

$$p_{ceq} = p_n - p_w \quad (2)$$

as the pressure difference between the wetting-phase pressure, p_w , and the nonwetting-phase pressure, p_n .

[3] Equation (1) is a pore-scale description that is often used in theoretical analyses and pore network modeling to distribute two immiscible fluid phases within the network [Wilkinson, 1986; Ioannidis *et al.*, 1991; Dullien, 1992; Reeves and Celia, 1996; Held and Celia, 2001]. Equation (2), on the other hand, is a macroscopic relationship used in laboratory experiments on soil and rock cores to relate measurements of the nonwetting- and wetting-phase fluid pressures to concurrent measurements of saturation, S . For multiphase flow, a macroscopic capillary pressure–saturation relationship provides one of the constitutive relationships [Bear and Verruijt, 1987] used to couple flow equations (e.g., modified Darcy's law) for each fluid phase in a porous medium. This constitutive relationship is

$$p_n - p_w = p_{ceq} = f(S) \quad (3)$$

[4] While this constitutive relationship is appealing, such descriptions of multiphase flow are not based on fundamental fluid dynamics, and are known to fail in many cases [Bear, 1972; Dullien, 1992; van Genabeek and Rothman, 1996; Muccino *et al.*, 1998]. In general, knowledge of the saturation of each phase is not sufficient to describe the state of the system. Numerous experimental investigations have shown that p_{ceq} is not a single-valued function of saturation,

¹Department of Physics, Purdue University, West Lafayette, Indiana, USA.

²Department of Earth and Atmospheric Sciences, Purdue University, West Lafayette, Indiana, USA.

³Now at Petroleum Abstracts, University of Tulsa, Tulsa, Oklahoma, USA.

but has a hysteretic relationship with the imbibition history of the system [Collins, 1961; Morrow, 1970; Topp, 1969; Colonna et al., 1972; Bear, 1979; Lenhard, 1992; Dullien, 1992]. Hence, capillary pressure cannot be determined simply from saturation or vice versa.

[5] In the past few decades, several investigators [Rapoport and Leas, 1951; Gvirtzman and Roberts, 1991; Bradford and Leij, 1997; Gray and Hassanizadeh, 1989, 1991, 1998; Hassanizadeh and Gray, 1990; Powers et al., 1991; Reeves and Celia, 1996; Deinert et al., 2005] have recognized that an accurate description of multiphase flow in a porous medium must account for the thermodynamics and the geometry of the interfaces between the fluids (and between the fluids and the solid phase). In that work, the physics of the interfaces enters as an interfacial area per volume, which, when combined with capillary pressure and saturation, is hypothesized [Hassanizadeh and Gray, 1990, 1993; Muccino et al., 1998] to lead to a unique description of the thermodynamic energy state. Cheng [2002], Cheng et al. [2004] and Chen et al. [2007] showed experimentally that the capillary-dominated interfacial area per volume does lift the ambiguity in the hysteretic relationship between capillary pressure and saturation. While saturation provides a description of the relative amounts of the fluids, interfacial area per volume between the wetting and nonwetting phase provides a partial description of the spatial distribution of the fluids.

[6] Thermodynamically based theoretical studies have proposed relationships among capillary pressure, p^c , saturation and interfacial areas between phases when multiple fluids are present in a porous medium [Morrow, 1970; Kalaydjian, 1987; Hassanizadeh and Gray, 1990, 1993; Deinert et al., 2005]. In their 1993 paper, Hassanizadeh and Gray proposed that capillary pressure, p^c , in thermodynamic equilibrium under uniform phase distribution, is related to interfacial areas per volume by

$$p^c = -s^w \rho^w \frac{\partial A^w}{\partial s^w} - s^n \rho^n \frac{\partial A^n}{\partial s^w} - \sum_{\alpha\beta} \frac{\gamma^{\alpha\beta}}{\phi} \left(\frac{\partial a^{\alpha\beta}}{\partial s^w} \right) \Big|_{T, \phi, \Gamma^{\alpha\beta}, A^{\alpha\beta}} \quad (4)$$

where $\gamma^{\alpha\beta}$ is the interfacial tension between phases α and β , $a^{\alpha\beta}$ is the interfacial area per volume between phases α and β , A^α is the Helmholtz free energy of phase α per unit mass of phase α , ρ^α is the mass of phase α per unit volume of α phase, ϕ , is the porosity, and s^w is the saturation of the wetting phase. The phases are represented by w for the wetting phase, n for the nonwetting phase and s for the solid phase. The porosity is represented by ϕ . The first and second terms in equation (4) explicitly include the dependence of the free energy on saturation, which would apply to the case of saturation gradients across the system. There is no term for free energy associated with the solid phase because it does not depend on saturation. Because of the fundamental presence of saturation gradients during the physical process of imbibition and drainage in a porous medium, these free energy terms may be anticipated to make important contributions.

[7] Expanding the last term of equation (4) gives the differential pressure contributions:

$$\sum_{\alpha\beta} \frac{\gamma^{\alpha\beta}}{\phi} \left(\frac{\partial a^{\alpha\beta}}{\partial s^w} \right) \Big|_{T, \phi, \Gamma^{\alpha\beta}, A^{\alpha\beta}} = \frac{1}{\phi} \left[\gamma^{wn} \frac{\partial a^{wn}}{\partial s^w} + \gamma^{ns} \frac{\partial a^{ns}}{\partial s^w} + \gamma^{ws} \frac{\partial a^{ws}}{\partial s^w} \right] \quad (5)$$

Equation (5) is derived from the change in free energy of the interfaces caused by a change in wetting-phase saturation and indicates that capillary pressure is a function not only of saturation but also depends on the interfacial area per volume between the fluid phases and between each fluid phase and the solid. Equation (5) requires each partial derivative to be taken at a constant temperature, T , medium porosity ϕ , interfacial mass density, $\Gamma^{\alpha\beta}$, and Helmholtz free energy of interface $\alpha\beta$ per unit mass of interface $\alpha\beta$, $A^{\alpha\beta}$. Only at equilibrium will equation (4) be equal to $p_n - p_w$ (equation (2)). The first term in equation (5) is the same as that proposed by Kalaydjian [1987] to be equal to p^c . In their study, Deinert et al. [2005] proposed a subset of the terms in equation (5) to be equal to p^c by defining the system to be confined to the wetting fluid and thus eliminated the term associated with the interfacial area between the nonwetting phase and the solid. These considerations raise important questions about the role played by the terms in equation (5), about the relative magnitude of the individual contributions of the individual terms in equation (4), and how or whether these are related to p^c .

[8] To date, the applicability of the relationships among capillary pressure, saturation and interfacial area per volume (such as that given by equation (5)) has not been tested via laboratory data that directly images interfaces between phases. In this paper, we use the results from imbibition and drainage experiments performed on two-dimensional micromodels to investigate the ability to calculate capillary pressure from measurements of interfacial area per volume and saturation. These experiments measure interfacial area, saturation and interfacial curvature with sufficient accuracy to explore the applicability of equations (4) and (5).

2. Experimental Details

[9] Measuring pore-scale and subpore-scale features requires measurement techniques that can probe interfacial area and pore geometry from the length scale of the pore to the length scale of a representative volume of the porous medium. Experimental methods that have been used to acquire measurements of interfacial area per volume on natural and synthetic samples include synchrotron-based X-ray microtomography [Culligan et al., 2004, 2006], photoluminescent volumetric imaging [Montemagno and Gray, 1995] and interfacial tracers [Saripalli et al., 1997; Annable et al., 1998; Kim et al., 1999a, 1999b; Anwar et al., 2000; Rao et al., 2000; Schaefer et al., 2000; Costanza-Robinson and Brusseau, 2002; Chen and Kibbey, 2006]. In this study, we use transparent two-dimensional micromodels to quantify fluid and interfacial distributions to investigate the robustness of capillary pressure calculations from interfacial information. The admitted disadvantage of using micromodels is that they are inherently two-dimensional systems. However, these are the only systems that enable direct visualization and quantification of interfaces with such high resolution. A general review of two-dimensional micromodels is given by Giordano and Cheng [2001]. The details of our experimental approach can be found in work by Cheng [2002], Cheng et al. [2004], Chen [2006], and Chen et al. [2007]. A general review of other techniques for producing micromodels is given by Giordano and Cheng [2001]. A detailed description of the procedures for

Table 1. Name, Size, Porosity, and Number of Images Analyzed for the Micromodels Used in This Study

Sample Name	Aperture, μm	Porosity, %	Number of Images Analyzed
S70	2.0	62.3	196
S1dc	1.0	70.3	411

performing optical lithography is given in the manufacturer's manual [Shipley, 1982] and in work by Thompson *et al.* [1994]. Below, we present a brief description of the experimental method to aid in the understanding of the results.

[10] The micromodels used in this investigation were constructed using optical lithography. A pore structure pattern is transferred under vis-UV illumination from a transparent mask to a photosensitive polymer layer called a photoresist. The thickness of the photoresist layer determines the depth of the flow channels. When a region of the photoresist is exposed to a sufficiently large integrated intensity of blue light, a photochemical reaction within the photoresist makes the region soluble in a developer solution. The unexposed photoresist is not soluble, so after development the photoresist layer contains a negative image of the original light pattern. For the micromodels in this study, we used Shipley photoresist types 1805 and 1827 with their standard developer [Shipley, 1982]. The micromodels were fabricated with pore networks covering a $600\ \mu\text{m} \times 600\ \mu\text{m}$ area. The pore structure for the micromodels was generated using a standard random continuum percolation construction [Nolte and Pyrak-Nolte, 1991]. Table 1 lists the name, the porosity and the depth (aperture) of the flow channels of the two micromodels shown in Figure 1. Model S70 has a $2\ \mu\text{m}$ aperture, while model S1dc has a $1\ \mu\text{m}$ aperture. The entrance pressure between these two micromodels differs by a corresponding factor of two.

The two different apertures of $1\ \mu\text{m}$ for model S1dc and $2\ \mu\text{m}$ for model S70 test for aperture-dependent systematics in the data.

[11] A pressure system was used to introduce two fluid phases into the micromodels. The system enables the simultaneous measurements of pressure and optical characterization of the geometries of the three phases (two fluid, one solid) within the sample. The apparatus contains a pressure sensor (Omega PX5500C1-050GV) to monitor the inlet pressure, and a video camera that is interfaced to an optical microscope to image the two-phase displacement experiments. The outlet is exposed to atmospheric pressure.

[12] To perform a measurement on a micromodel, the micromodel is initially saturated with decane, a wetting fluid, which is inserted from the outlet side. A second fluid, nitrogen gas, is introduced from the inlet. The initially decane-saturated micromodels are invaded with nitrogen by the incremental application of pressure. After each pressure increment, the system is allowed to reach mechanical equilibrium (typically 3–5 min) in which the interfaces are fully stationary, and the inlet pressure is recorded. Then the saturation and distribution of each phase are digitally imaged by a CCD camera through the microscope. The camera is a Qimaging Retiga EX with an array of 1360×1036 pixels that have a pixel size $6.45\ \mu\text{m}$ by $6.45\ \mu\text{m}$ with 12-bit digitization and FireWire (IEEE-1394) transfer. The microscope is an Olympus microscope with a $16 \times$ objective and is illuminated with a white light source through a red filter. The resulting digital images have a pixel resolution of $0.6\ \mu\text{m}$. All measurements are conducted at room temperature (temperature stability better than 0.5°C during a measurement), with the apparatus located within a clean bench environment. Sample S70 was sent through several imbibition and drainage scanning cycles under a total of 196 pressures. Sample S1dc was similarly subjected to scanning cycles under 411 different pressures. An image was captured and analyzed for each pressure. An archive of the images used in this study has been placed on a website for

(a) S70 - Aperture 2 microns



(b) S1dc - Aperture 1 micron

**Figure 1.** Digital images of micromodels (a) S70 and (b) S1dc. In the images, nitrogen is white, and photoresist (solid) is dark gray.

Table 2. Sample Name and IDL Parameters Used in the SEARCH2D Command to Analyze the Mask for Samples S70 and S1dc

Sample Name	X_{pos}, Y_{pos}	Min_Val	Max_Val
S70	700, 10	115	255
S1dc	700, 10	75	255

downloading (see data by L. J. Pyrak-Nolte, 2007, <http://www.physics.purdue.edu/rockphys/DataImages/>).

3. Analysis

[13] To determine capillary pressure from either equation (1) or equation (5) requires the identification of each phase (decane, nitrogen, solid) and all the interfaces between the phases. Image analysis programs are coded in the IDL language to extract phase saturation, interfacial area per volume (IAV), and curvature of the interfaces from each image. In the analysis, each gray scale image is separated into three separate images, i.e., one binary image representing each phase. The individual phase images are used to determine the saturation of the micromodel for each phase. The fraction of the micromodel composed of photoresist (i.e., the solid portion of the micromodel where no flow occurs) is constant for all drainage-imbibition cycles. Nitrogen and decane saturations of the pore space are calculated as a fraction of total pore space.

[14] A mask was used to separate gray scale images into three separate phase images. The mask was a gray scale image of the micromodel filled only with nitrogen (e.g., Figure 1). A two-dimensional search algorithm (command SEARCH2D in IDL) was used to find the connected pore space in the model and to determine the regions of photoresist. The SEARCH2D command starts at a specified location (X_{pos}, Y_{pos}) within the array and finds all data that fall within a specified intensity range ($Min_Val \leq data \leq Max_Val$) and that are connected. Table 2 lists the values of X_{pos} , Y_{pos} , Min_val , and Max_Val used in the analysis of the masks for samples S70 and S1dc. For both S1dc and S70, the DIAGONAL keyword is used to have the algorithm search all surrounding data points that share common corners. This analysis results in the generation of a new mask that is a binary image with regions representing pore space set equal to one and those regions representing photoresist set equal to zero.

[15] An autocorrelation method was used to align and register the new mask with each image from the drainage and imbibition experiments to ensure that the same region of the micromodel is analyzed for all images. After alignment, the gray scale images for each saturation, originally 1520 pixels by 1180 pixels, were cropped to 1000 pixels by 1000 pixels. The SEARCH2D algorithm was then performed on each cropped gray scale image (for each pressure value) to determine the connected nitrogen phase. The connected nitrogen phase was set to a value of 255 and a new image was created. By multiplying the new image by the new mask and searching for all values equal to 255, the phase image for nitrogen is determined. The IDL DILATE command was used on the nitrogen image to algorithmically determine the boundary between nitrogen and the other

phases because optical refraction affects the images the interfaces between nitrogen and the other two phases. A 3×3 structure array (with all elements equal to 1) was defined and applied to the nitrogen image through the DILATE command. Without this step, the nitrogen phase did not match the original image because of an apparent rim around the nitrogen phase caused by the diffraction of light from the nitrogen interfaces, or possibly caused by the hidden curvature. The rim around the nitrogen phase can be seen in Figure 2f which is an enlargement of a portion (300 pixels by 300 pixels) of image 94 shown in Figure 2a for sample S70.

[16] Using the IDL WHERE command, the location of the photoresist in the mask was determined and those locations in the new image are set equal to zero. The phase image for photoresist is defined as the pixels in the new image equal to zero. Regions not equal to 0 or 255 are then defined to be decane and the phase image for decane is produced. Figure 2a is a gray scale image from S70 (image 94) partially filled with nitrogen. After applying the imaging processing techniques just described, the three binary images for Figure 2a are produced and are shown in Figures 2b, 2c, and 2d for photoresist, decane and nitrogen, respectively. A false color composite image is shown in Figure 2e on the basis of combined binary images. A weighting was given to each image to form the false color composite image (nitrogen*30, decane*5, photoresist*1) shown in Figure 2e.

[17] Once the saturation of each phase was established, the interfacial length of each interface was determined. Three interfacial lengths are calculated (1) between nitrogen and decane (wn), (2) between decane and photoresist (ws), and (3) between nitrogen and photoresist (ns). Sobel and thinning operators were applied to each individual phase image at a given nitrogen pressure, and the length of each interface was totaled. At this stage in the analysis, the interfacial length from an individual phase image contained the phase in contact with each of the other phases. For example, for a nitrogen phase image, both the interface between nitrogen and decane and nitrogen and photoresist were included. The interface between two phases was then obtained through the following relationships:

$$\begin{aligned} L_{wn} &= (L_n + L_w - L_s)/2 \\ L_{ns} &= (L_n + L_s - L_w)/2 \\ L_{ws} &= (L_w + L_s - L_n)/2 \end{aligned} \quad (6)$$

where is L_n is the total length of the nitrogen interface, and L_w and L_s are the total lengths of the decane and photoresist interfaces, respectively. L_{wn} is the length of the interface between nitrogen and decane. L_{ns} is the length of the interface between nitrogen and photoresist. L_{ws} is the length of the interface between decane and photoresist. In this study, we calculate interfacial length per area (ILA) because the hidden curvature associated with the aperture cannot be obtained from the two-dimensional image (although we estimate its contributions in equation (8) below). Though we calculate ILA, we will refer to it as either interfacial area per volume (IAV) or by the term $a^{\alpha\beta}$, where α and β give the phases (w for wetting phase, n for nonwetting phase or s for solid) between which the interface occurs. The interfacial area per volume is found by dividing L_{wn} by

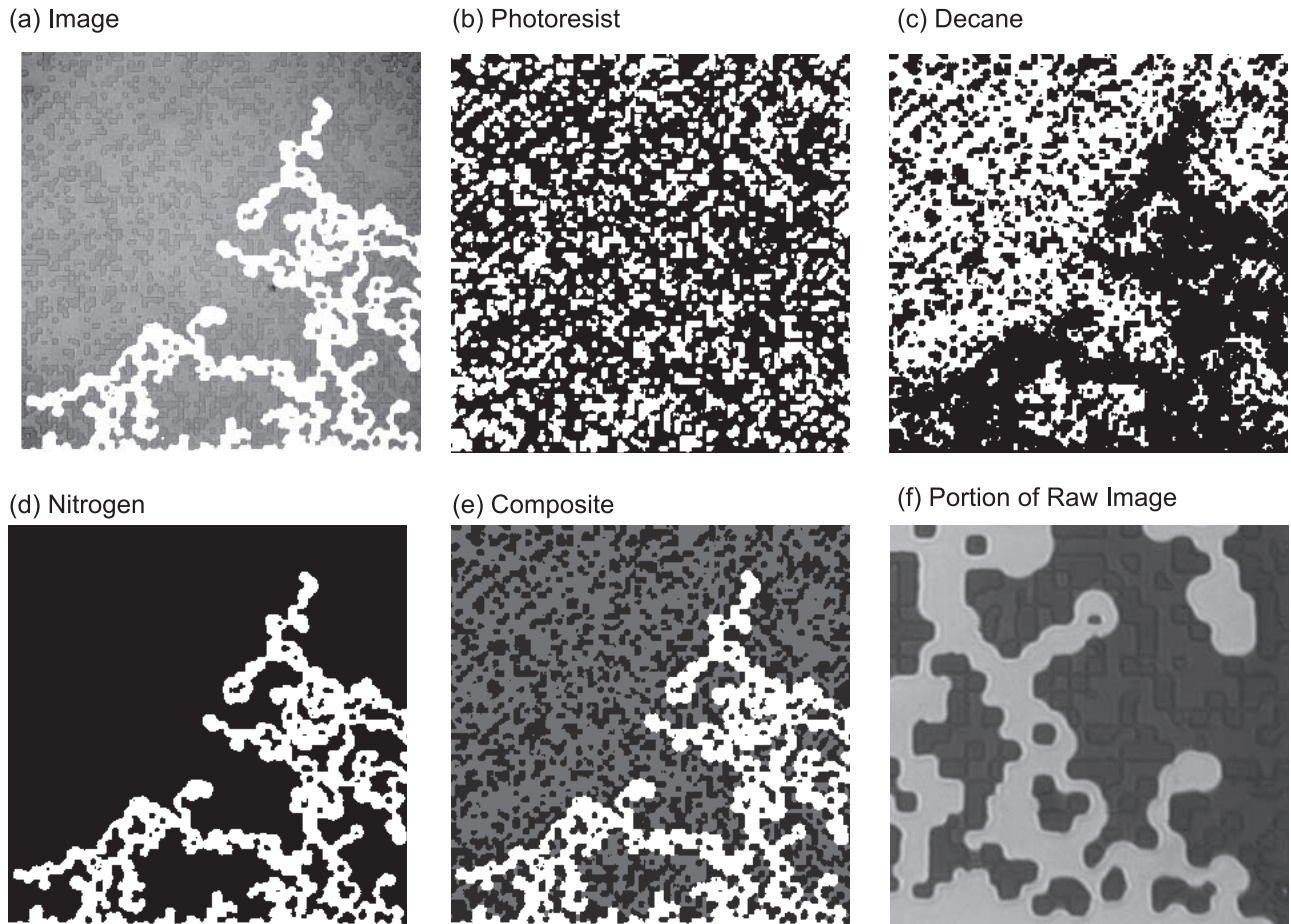


Figure 2. (a) Digital image of sample S70 partially filled with nitrogen (image 95). Binary images of (b) photoresist (white regions), (c) decane (white regions), and (d) nitrogen (white regions). (e) Composite of Figures 2b, 2c, and 2d. In Figure 2e, white represents nitrogen, gray represents decane, and the photoresist is shown in black. (f) An enlargement of a portion (300 pixels by 300 pixels region) of image 94 shown in Figure 2a.

the total area of the micromodel (600 μm by 600 μm) giving units of inverse length.

[18] *Chen* [2006] and *Chen et al.* [2007] determined the error in IAV and saturation by applying the analysis technique to circles of known radii and squares with known perimeters and areas. For circles with radii greater than or equal to 4 pixels (2.4 μm), the numerically determined values of IAV were less than 10% of that calculated from $2\pi r$. This is caused by the pixilation of the circle, i.e., a circle made up of small squares. For the same set of circles, the calculated area of the circle versus the area determined from counting pixels were within 2.5% for circles with radii greater than or equal to 4 pixels. For circles with radii between 1 pixel and 4 pixels the error in area and IAV ranged from -20% to 3% , respectively. For the squares, the relative error between the estimated and the known perimeter of the squares is the largest (-30% to -10%) when the edge length is less than 4 pixels but decreases quickly ($\sim 5\%$ at 6 pixels) as the perimeter increases. Other methods exist for determining interfacial areas [e.g., *Dalla et al.* [2002]; *McClure et al.*, 2006; *Prodanovic et al.*, 2006] that might reduce the error, but at this time we chose the simplest analysis method. An archive of the images used in this study have been placed on a website for downloading so other

researchers can investigate these issues (see <http://www.physics.purdue.edu/rockphys/DataImages/>).

[19] The error caused by the hidden curvature along the z axis cannot be measured directly, but can be estimated on the basis of the known contact angle of decane on photoresist in nitrogen. The total area of an interface with two principle radii $R_1 \ll R_2$ is given by

$$A = 4R_1R_2 \left(\frac{\pi}{2} - \theta_c \right)^2 \quad (7)$$

where θ_c is the contact angle. The relative error in this area, caused by the hidden contact curvature that cannot be measured directly, is

$$\frac{\Delta A}{A} = \frac{4\pi R_1 R_2 \Delta \theta_c}{\pi^2 R_1 R_2} = \frac{4}{\pi} \Delta \theta_c \quad (8)$$

which is independent of the radii. For decane on photoresist in air, the contact angle is $\theta_c = 0.08$ rad. Assuming an error no larger than the contact angle itself (100% change in contact angle), this leads to a maximum error in the calculated interfacial area of about 13%. This is a worst case value, and practical values of the error are likely to be

smaller. Therefore, the hidden curvature in the two-dimensional micromodels is not a large source of error and is no larger than the pixel errors.

[20] We adapted a level set method [Sethian, 1985] to calculate capillary pressure using the curvature of the interface between the wetting and nonwetting phases from the images. The curvature of an interface is obtained from the image using

$$K = \frac{\Phi_y^2 \Phi_{xx} - 2\Phi_x \Phi_y \Phi_{xy} + \Phi_x^2 \Phi_{yy}}{(\Phi_x^2 + \Phi_y^2)^{3/2}} \quad (9)$$

where K is the curvature of the interface, i is the derivative of the image with respect to i where i is either x or y , Φ_{ii} is the second derivative of the image with respect to ii , where ii can be xx , yy or xy . The derivatives of the two-dimensional images are taken using a kernel method. The kernels (as used in IDL) are defined as

$$\begin{aligned} \Phi_x &= [-0.5, 0, 0.5] \\ \Phi_y &= \text{transpose}[\Phi_x] \\ \Phi_{xx} &= [1.0, -2.0, 1.0] \\ \Phi_{yy} &= \text{transpose}[\Phi_{xx}] \\ \Phi_{xy} &= \begin{bmatrix} 0.25 & 0 & -0.25 \\ 0 & 0 & 0 \\ 0.25 & 0 & -0.25 \end{bmatrix} \end{aligned} \quad (10)$$

Because of discontinuities in the image densities, the level set analysis is performed on the phase images convolved with a 19-pixel Gaussian blur of the image. This provides a gray scale or gradient at each interface to allow derivatives to be taken, after which these images are convolved with the kernel. Once the curvature is computed, a mask of the interface relevant to each phase is applied. We use the curvature of only the capillary-dominated interfaces to assess the capillary pressure. The MOMENT command in IDL is used to compute the average curvature for an image. The MOMENT command calculates the mean value on the basis of the values of curvature along each interface, i.e., only the values for pixels representing the wetting-nonwetting interfaces in an image. The most probable curvature is calculated from the histogram of curvatures for a single image with the value of curvature from the peak of the distribution representing the mode of the curvature.

[21] Computation of the normals to the interfaces was also performed. The calculation of the normals begins by using the equation

$$\begin{aligned} n_x &= \frac{\Phi_x}{\sqrt{\Phi_x^2 + \Phi_y^2}} \\ n_y &= \frac{\Phi_y}{\sqrt{\Phi_x^2 + \Phi_y^2}} \end{aligned} \quad (11)$$

and then applying the convolution

$$\begin{aligned} n_{xx} &= \text{Image} * n_x n_x \\ n_{yy} &= \text{Image} * n_y n_y \\ n_{xy} &= \text{Image} * n_x n_y \end{aligned} \quad (12)$$

where n_{xx} , n_{yy} and n_{xy} are the normals to the interfaces, and “image” refers to the two-dimensional image of the interface between two phases.

[22] Equation (5) requires the calculation of the differential of the interfacial area with respect to saturation at constant energy. In laboratory experiments, it is difficult to ensure that the condition of constant energy is met. In the micromodel experiments, each image is in mechanical equilibrium at a constant pressure, but different images with the same measured capillary pressure have different saturations and do not have equal free energy because of the hysteresis in the $p^c - s^w$ relationship. Therefore, the three partial derivatives in equation (5) must be evaluated from a single image of the micromodel at a given p^c . To accomplish this, we used a “microensemble” approach (Figure 3), in which values of s^w and a^{wn} are calculated from a single image on the basis of subsets of the image. The microensemble analysis is performed on all 196 images for sample S70 and all 411 images for sample S1dc because one image represents one value of p^c . A window 980 pixels wide by 300 pixels in length is moved in 1 pixel increments from the inlet to the outlet of the sample (a distance of 680 pixels out of 980 pixels). We choose a representative elementary volume (REV) in which the porosity of the region was relatively constant. The micromodels were based on random percolation patterns. If the REV was too small, the porosity of the REV fluctuated along the length of the sample. For example, with a window length of 200 pixels, the porosity varied 10% along the length of a sample. With a window of 300 pixels, the variation in the porosity along the length of the sample was roughly 1.5%. For each subset of the image, the values of s^w , s^n , a^{wn} , a^{ns} and a^{ws} are calculated. The differentials ($da^{\alpha\beta}/ds^w$) in equation (5) are determined from the slope of a line fit to the appropriate $a^{\alpha\beta}$ versus s^w graph. These values are used to calculate the individual terms in equation (5) using the values of interfacial tension given in Table 3, to calculate the contribution to capillary pressure from the energy associated with interfaces.

4. Results and Discussion

4.1. Mechanical Equilibrium

4.1.1. Capillary Pressure From Curvature

[23] In Figure 4, the capillary pressure calculated from the curvature of the interface between the wetting and nonwetting phase is shown as a function of the externally measured pressure (external to the porous structure) for the two micromodels listed in Table 1 and shown in Figure 1. The calculated values are the entry pressure plus the increment in pressure above the entry pressure needed to invade the pore structure of the sample. The entry pressure for a 2 μm deep channel is 23.8 kPa when the surface tension between the two fluids is 23.8×10^{-3} N/m. For the 1 μm deep channels, the entry pressure is 47.6 kPa. Also shown in the Figure 4 is a line with unity slope. This line is given as guide for comparing the change in pressure determined from the interfacial curvature to that recorded by the pressure transducer. Other investigators [Philip, 1977; Tuller *et al.*, 1999] have shown theoretically that the curvature of interfaces between two immiscible fluids is affected by adsorbed wetting films between the nonwetting phase and the solid. In our analysis, we treated the phe-

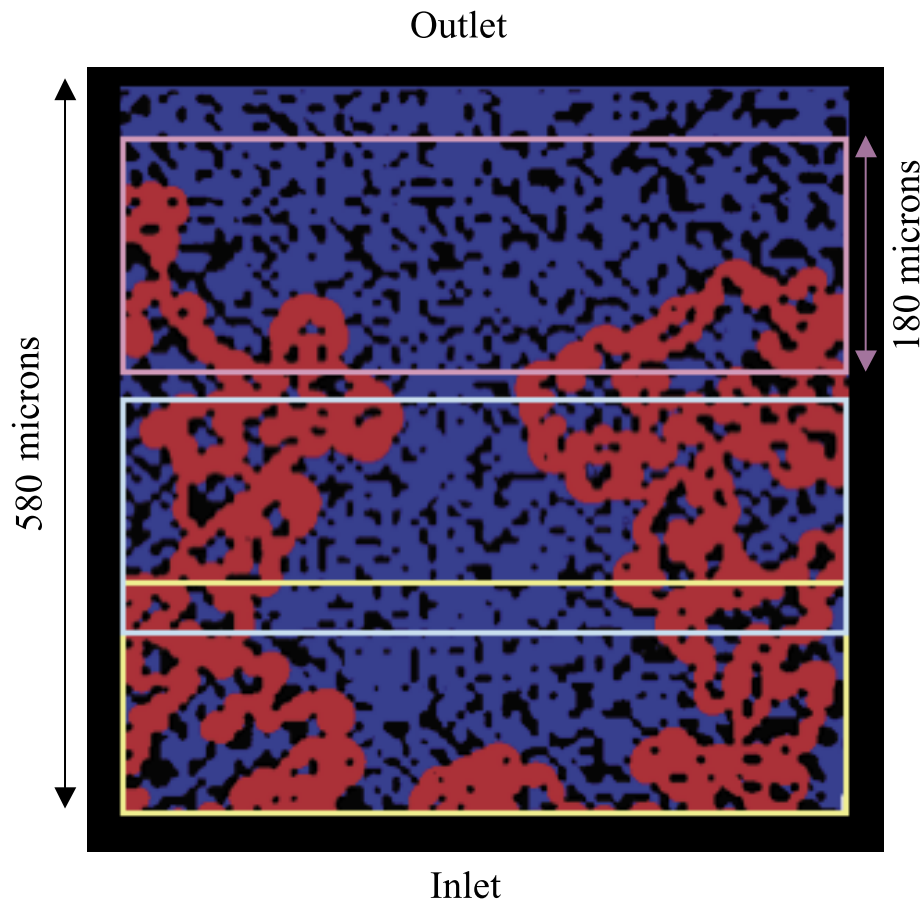


Figure 3. Schematic of moving-window technique (microensemble approach) using a false color image (image 42) from sample S1dc. The window is shown at three different locations by the rectangles outlined in yellow, light blue, and pink. The width of the window matches the width of the micromodel (980 pixels or $\sim 600 \mu\text{m}$), and the length of the window is approximately 300 pixels ($\sim 180 \mu\text{m}$).

nomenon as purely capillary because the presence of films is below the image resolution.

[24] For any given image, the capillary-dominated interfaces do not exhibit a delta function distribution of curvatures. Instead, the histogram of the curvature distribution for a single image has a finite width [Cheng *et al.*, 2004]. Thus, in Figure 4, two values are presented. These are the pressures based on average curvature of all of the wetting-nonwetting interfaces, and the mode (or most probable) curvature of these interfaces in an image. Using either value, a reasonable agreement between the calculated pressure and the measured pressure is observed for samples S70 and S1dc. The values from the average and the mode agree well with each other in sample S70 ($2 \mu\text{m}$ aperture), but they separate a little for sample S1dc with the smaller aperture ($1 \mu\text{m}$ aperture). The average tends to be slightly more stable than the mode, and the average is used in the remaining figures.

[25] The average curvature as a function of distance from the inlet was calculated to determine if the fluids in the image were in mechanical equilibrium by measuring whether the curvature-based capillary pressure is constant throughout the sample for each image. The variation of capillary pressure (Figure 5a), wetting-phase saturation, s^w , (Figure 5b) and interfacial area per volume (a^{wn} Figure 5c) are shown as functions of distance from the inlet for image

42 (shown in Figure 3) of sample S1dc. The capillary pressure (Figure 5a) is nearly constant with distance from the inlet, which further supports the conclusion that the system is indeed in mechanical equilibrium. However, s^w and a^{wn} do vary along the length of the sample. There is clearly a saturation gradient along the inlet-outlet direction. Such a gradient is a fundamental property of all imbibition-drainage processes in which the porous medium is attached to source-sink reservoirs.

[26] Figure 6 shows the capillary pressure based on curvature plotted in an alternate way as a function of wetting-phase saturation for image 42 (shown in Figure 3) of sample S1dc. Within experimental error, the capillary pressure is not a function of s^w even though s^w and a^{wn} both vary along the length of the sample. Figure 7a shows the histogram of the pressure gradient and Figure 7b gives the histogram of the coefficient of variance (CV) of the

Table 3. Interfacial Tensions Between Phases in the Micromodel

Interface	Interfacial Tension, mN/m
Decane-nitrogen	$\gamma^{wn} = 23.8$
Nitrogen-photoresist (PMMA)	$\gamma^{ns} = 40.6$
Decane-photoresist (PMMA)	$\gamma^{ws} = 2.2$

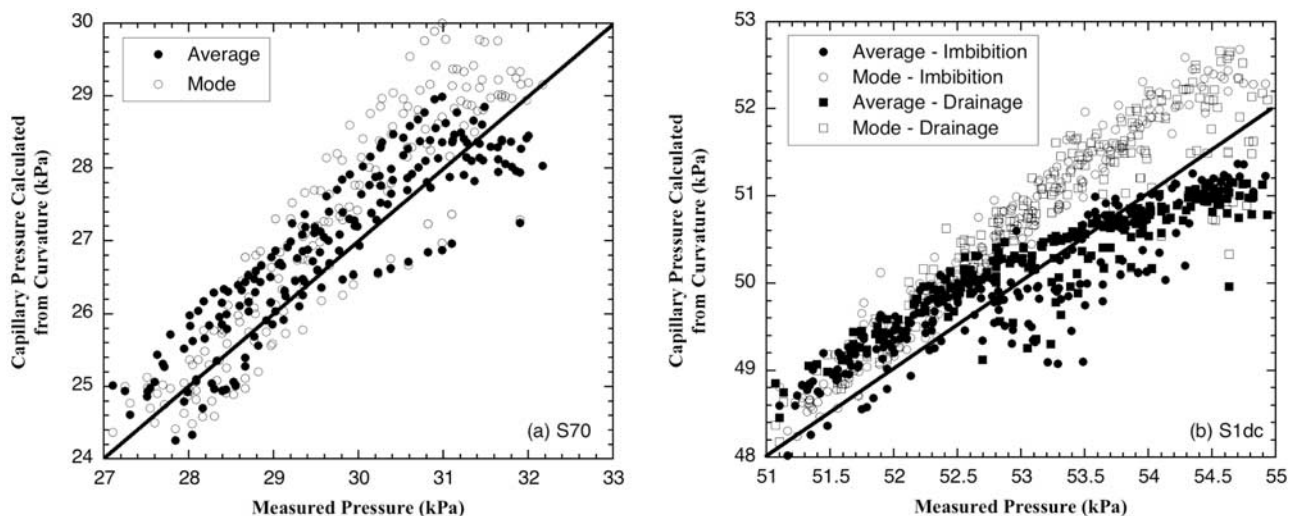


Figure 4. Capillary pressure calculated from equation (1) as a function of measured capillary pressure for micromodel samples (a) S70 and (b) S1dc.

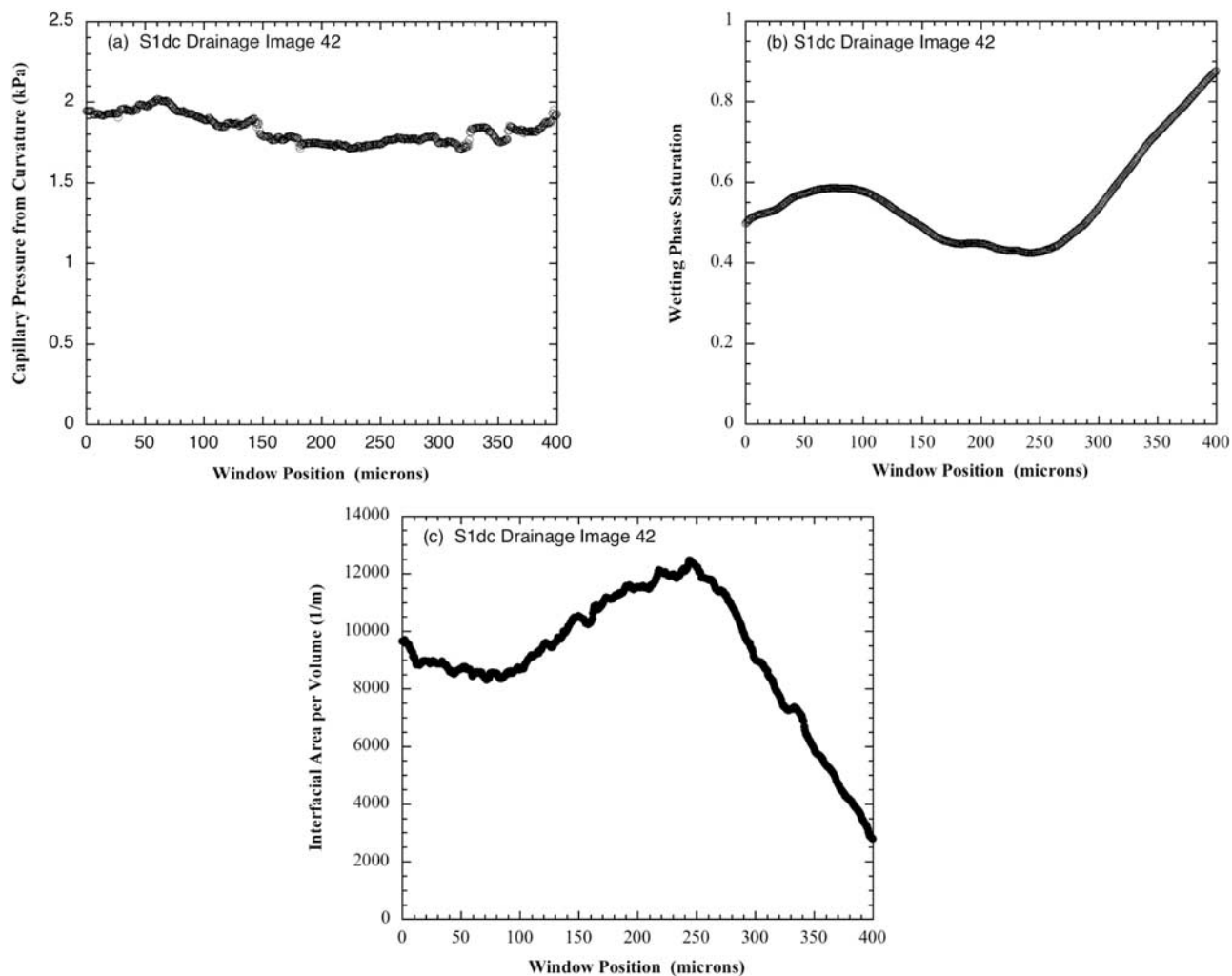


Figure 5. (a) Capillary pressure calculated from equation (1), (b) wetting-phase saturation, and (c) interfacial area per volume for the wetting-nonwetting interface for image 42 from sample S1dc as a function of distance from the inlet of the moving window. The moving window was approximately 180 μm in length.

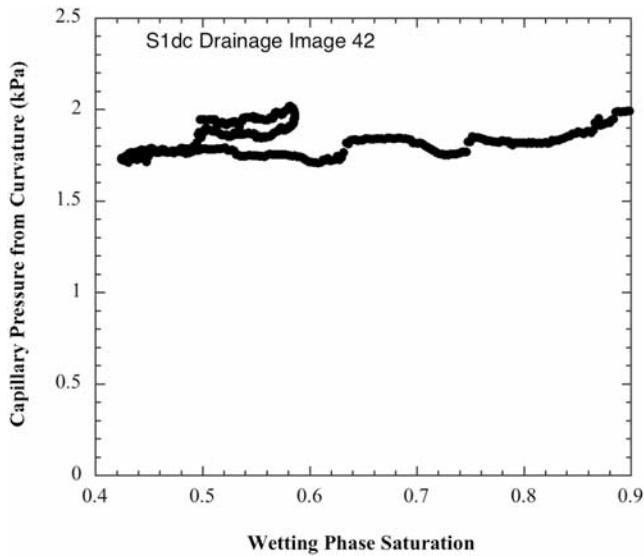


Figure 6. Capillary pressure calculated from equation (1) as a function of wetting-phase saturation for image 42 from sample S1dc on the basis of the microensemble approach.

pressures for all 205 images that compose the data set for drainage scanning of sample S1dc. The CV is calculated by taking the standard deviation of the capillary pressures and dividing by the mean capillary pressure value for that image. The pressure gradient is nearly zero (Figure 7a), and the capillary pressure is constant for most images to within 10%, which is consistent with each sample image at a given pressure having established mechanical equilibrium.

[27] Another check on mechanical equilibrium is the examination of the mean values of the surface normals for the interface between the wetting and nonwetting phase. Figure 8 shows the calculated values of the normal to the interface on the basis of equations (10) and (11) for the interface between the wetting and nonwetting fluid phases for sample S70 (Figure 8a) and sample S1dc for drainage scanning (Figure 8b) and imbibition scanning (Figure 8c)

for all images. In the homogeneous thermodynamic limit, a random orientation of interfaces would yield a value 0.5 for n_{xx} and n_{yy} and a value of zero for n_{xy} [Gray and Miller, 2006]. The data show that n_{xx} and n_{yy} are indeed approximately 0.5 for all wetting-phase saturations less than 0.9. The value of n_{xy} is about 0.05 for both samples and approaches zero as the wetting-phase saturation approaches 1. On the other hand, for saturations greater than 0.9, the normals, n_{xx} and n_{yy} are not random. This deviation from randomness at wetting-phase saturations greater than 0.9 occurs when the nitrogen is first entering the model from the inlet. Above 90%, the phase distribution is anisotropic and sensitive to initial conditions as the invading nitrogen fingers compete before one dominates. These data suggest that the individual terms in equation (5) can be safely evaluated for wetting-phase saturations below 90%.

4.1.2. Capillary Pressure From Interfacial Area Per Volume

[28] To calculate the contribution to capillary pressure from the interfaces between phases based on equation (5), the changes in a^{wm} , a^{ns} , and a^{ws} with wetting-phase saturation were calculated for each constant pressure image (the number of images for each sample is given in Table 1). Examples of the relationship between $a^{\alpha\beta}$ and s^w are shown in Figure 9. For each of the three interfaces, the dependence on s^w is highly linear. The slopes of the curves were taken and used in equation (5). In Figure 10, the capillary pressure calculated using equation (5) is shown along with each individual term in equation (5) for samples S70 and S1dc as functions of average capillary pressure calculated from the curvature of the interface. In Figure 10, only the increments in pressure above the entry pressure are used in the comparison. We use the average capillary pressure calculated from curvature because, as shown in Figure 3, it provides a reasonable match to the externally measured capillary pressure, while being a more faithful representation of the internal pressures in the micromodels.

[29] If only the first term of equation (5) were used, as suggested by Kalaydjian [1987], the calculated contribution to capillary pressure from interfacial area per volume

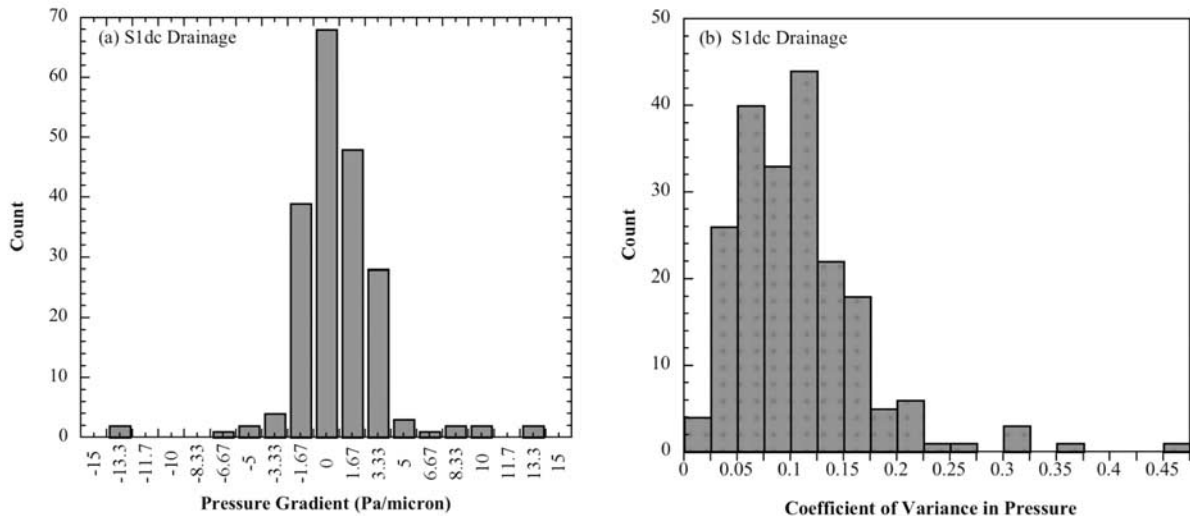


Figure 7. (a) Histogram of the pressure gradient and (b) histogram of the coefficient of variance in the pressure for 205 images from sample S1dc during drainage scanning.

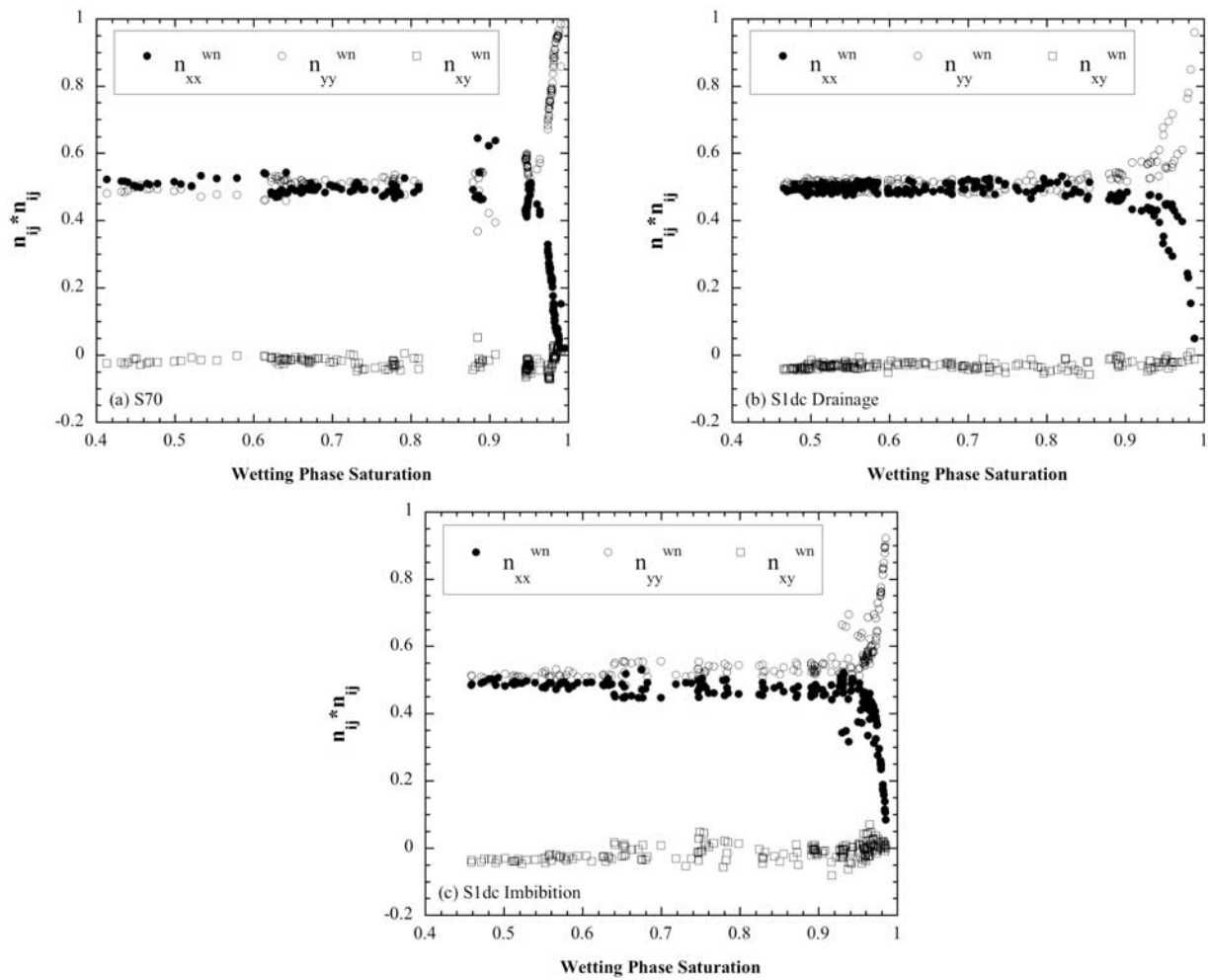


Figure 8. Average normals to the interfaces between wetting (decane) and nonwetting (nitrogen) as a function of wetting-phase saturation for (a) sample S70 and sample S1dc (b) drainage and (c) imbibition scanning.

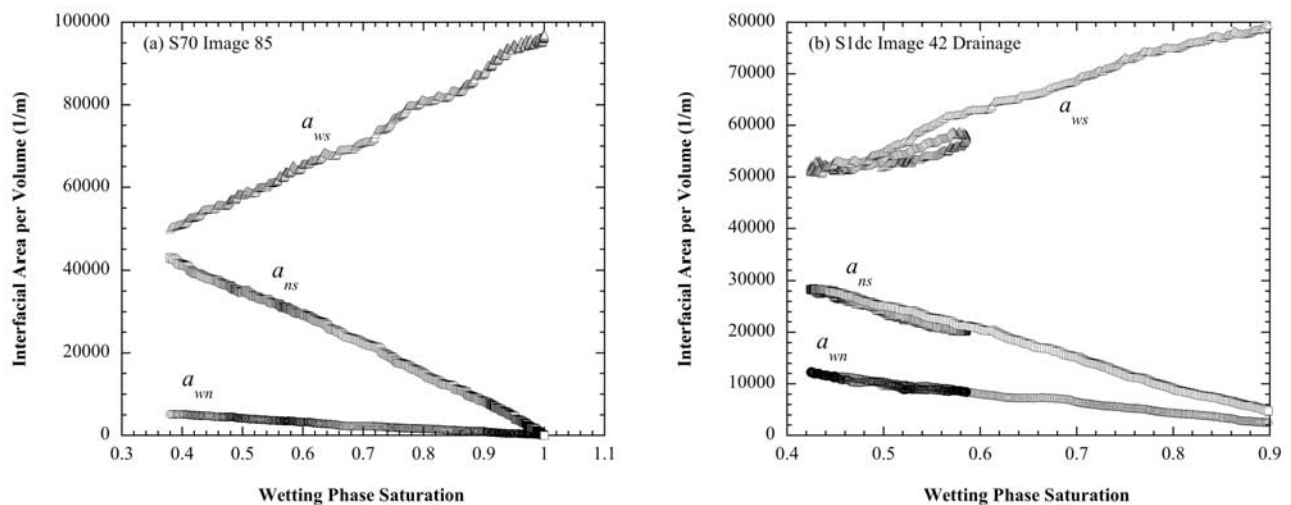


Figure 9. Change in interfacial per volume (a^{wn} , a^{ns} , and a^{ws}) as a function of wetting-phase saturation for (a) image 85 from sample S70 and (b) image 42 from sample S1dc drainage.

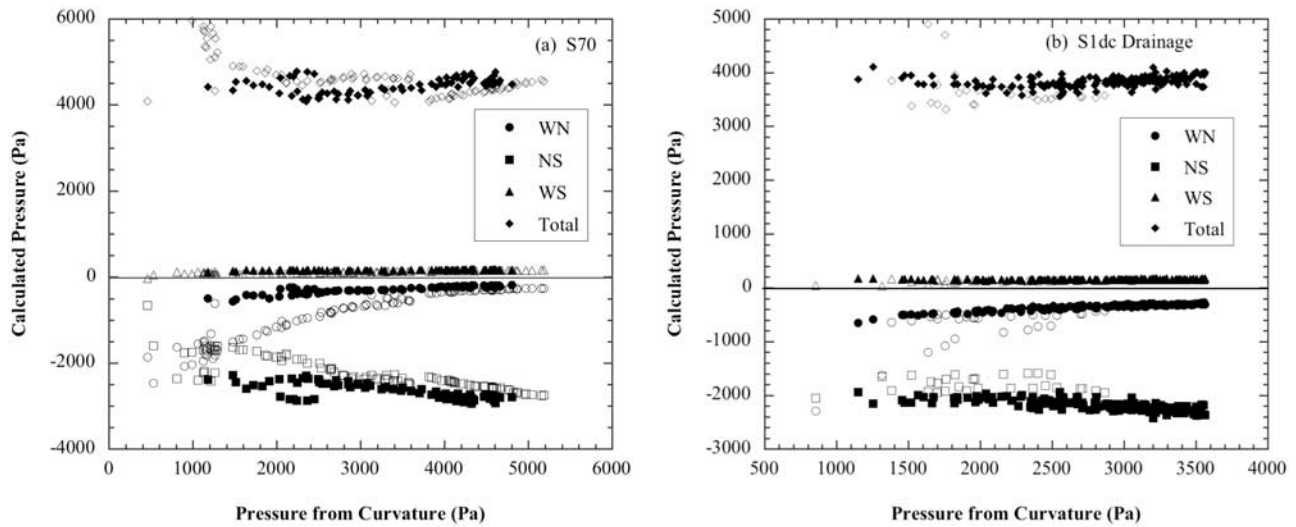


Figure 10. Capillary pressure based on equation (5) as a function of capillary pressure determined from curvature for samples (a) S70 and (b) S1dc from drainage scans. Shown in the graphs are the contributions from each term in equation (5) indicated by the interface (WN, wetting-nonwetting interface; WS, wetting-solid interface; NS, nonwetting-solid interface). The total represents the sum of all of the terms divided by the porosity as given by equation (5). The open symbols present the value of the term for wetting-phase saturations greater than 90%.

(circles in Figure 10) would actually decrease with increasing pressure. Examining the other terms in equation (5), though the a^{ws} is large in magnitude, da^{ws}/ds^w (triangles) is small because the value of the interfacial tension between the decane and the solid is an order of magnitude smaller than that for the other interfaces (Table 3). The da^{ns}/ds^w term (squares) increases with increasing pressure and dominates in magnitude. The total of all three terms (diamonds in the Figure 10) in equation (5) are also shown. The data arising from high wetting-phase saturations above 90% are shown separately (open symbols in Figure 10), because these data may not be applicable for the reasons described earlier. When only the $s^w \leq 0.9$ data (solid symbols in Figure 10) are considered, the component of capillary pressure calculated from the last term of equation (4) is found to be constant even though the pressure calculated from curvature is increasing. Therefore, the component of capillary pressure based on changes in interfacial area per volume with saturation given by the last term in equation (4) does not match the pressure determined from the average curvature of the wetting-nonwetting interfaces. This suggests that contributions to capillary pressure from the free energy associated with the saturation gradient of each phase (first and second terms in equation (4)) are not negligible.

4.2. Saturation Gradients

[30] From the data showing the uniform curvature distributions and phase isotropy for each image, combined with the interface stability (they are not moving), we conclude that the micromodels at each pressure are in mechanical equilibrium. However, from Figures 5a and 5b, it is clear that the phase distribution is not homogenous either in terms of amount (s^w) or distribution (a^{wn}) at a given pressure. These saturation gradients likely cause the contributions from the first two terms of equation (4) to dominate the calculation of capillary pressure, thereby producing the difference between the curvature-based pres-

sure of equation (1) and the terms associated with the interfaces in equation (5).

[31] From our data set, we cannot obtain all parameters used to determine contributions to capillary pressure from the change in Helmholtz free energy of a phase with saturation as given by equation (4). But we can plot the difference between equation (1) and equation (5) to obtain a residual contribution to the capillary pressure that is a consequence of the saturation gradient. This difference is shown in Figure 11 as a function of the curvature-based capillary pressure. We identify this difference as the saturation gradient contribution, and tentatively assign it to the explicit free-energy terms in equation (4). The free energy contribution takes on negative values at low pressure, and decreases in magnitude toward zero under higher pressures. At pressures approaching breakthrough, the free-energy contribution vanishes. It is interesting to note that the phase distribution across the sample is most nearly homogeneous just prior to breakthrough. This observation lends plausibility to the interpretation of the free-energy contribution arising from the saturation gradient.

5. Conclusions

[32] We have performed an experimental study using transparent two-dimensional micromodels that enable the visualization of interfacial areas during imbibition and drainage. These data provide a direct means to compare experimentally measured capillary pressure, determined either by local curvature or by external pressure measurements, to thermodynamic expressions involving the differential change of interfacial areas, also measured experimentally, relative to changing saturation. The mechanical equilibrium of the system is verified using several different measures, including the establishment of stationary phase fronts prior to data acquisition, the existence of near-zero pressure gradients across the sample for a given

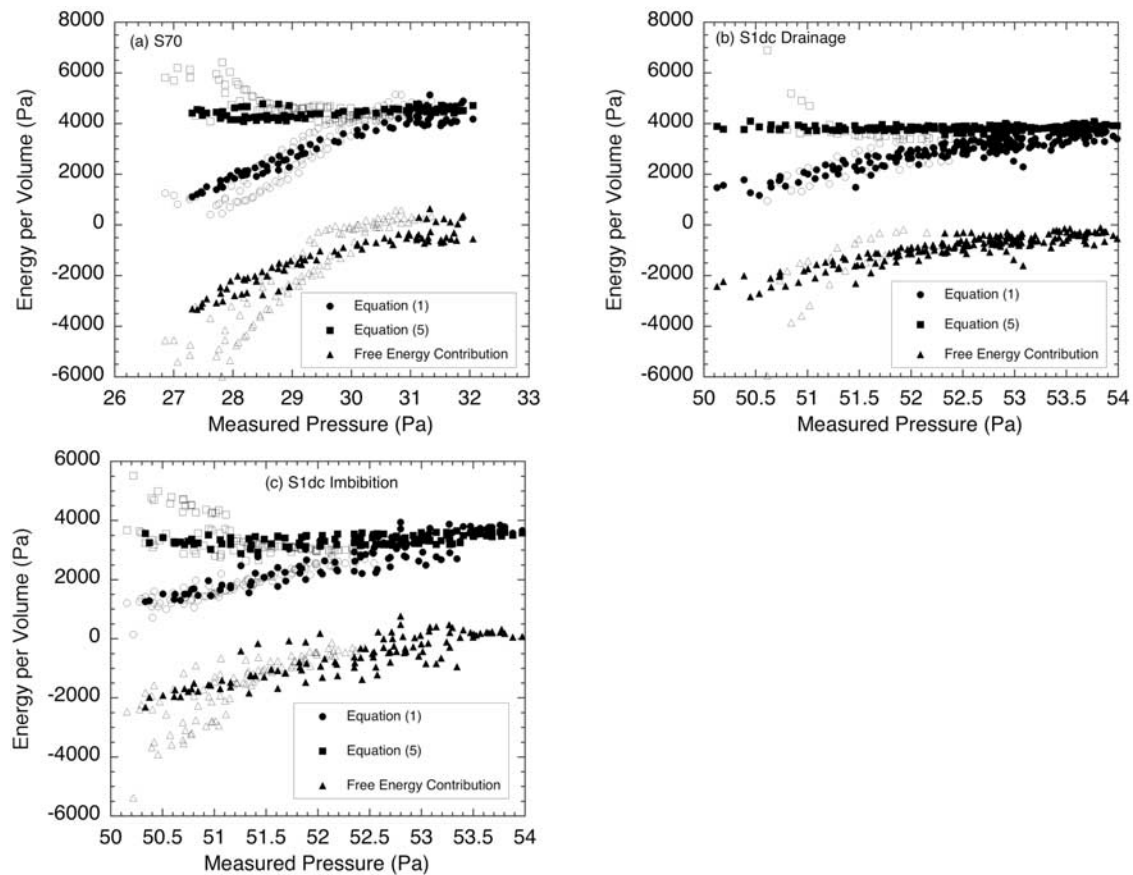


Figure 11. Energy per volume (in Pa) as a function of externally measured capillary pressure for (a) sample S70 and for sample S1dc (b) drainage scanning and (c) imbibition. The squares represent values based on equation (5). The circles represent the values based on equation (1). The triangles represent the contribution from inhomogeneous phase distribution. The open symbols represent the results for wetting phase saturations greater than 90%.

applied external pressure, the agreement between the pressure calculated from curvature and the pressure measured externally, and the vanishing surface normals for saturations below 90%. Above 90%, there is significant anisotropy as several invading nitrogen fingers compete. The data below 90% apply to the case when one, or at most two, nitrogen fingers dominate the invading phase distribution.

[33] In spite of the mechanical equilibrium established at each external pressure, each of the three terms in equation (5) that relate the differential change in interfacial areas per volume to the capillary pressure are found to be roughly constant for saturations below 90%. The combined contributions are likewise independent of the capillary pressure. The most likely cause of this difference is the saturation gradient that exists at all pressures along the inlet-outlet direction. Such saturation gradients can contribute additional terms, most likely related to the free energy of the system, that are nonzero under these conditions, but which would vanish in the case of homogeneous phase distribution.

[34] These results raise an important question about the nature of imbibition and drainage. The question is whether the saturation gradient indicates that the system is out of thermodynamic equilibrium, or whether the communication of the porous medium with inlet and outlet reservoirs allows

the existence of saturation gradients even under thermodynamic equilibrium.

[35] We argue that saturation gradients are a fundamental property of imbibition and drainage processes. Many important applications fall in this category, including borehole tests, oil well production, water wells, the study of cores in the laboratory, and micromodel experiments. In all these examples, the invading phase enters the micromodel from an inlet port attached to a reservoir and drains into an outlet reservoir. The inlet reservoir is a part of the equilibrium system, and the porous medium cannot be isolated from it as a closed system. This situation is fundamentally different than equilibrium bulk phase distributions in closed systems, in which pores of appropriate apertures are occupied homogeneously. Therefore, imbibition and drainage represent a class of open physical processes which are inhomogeneous because of the communication of the porous medium with the reservoirs that impose inlet-outlet asymmetry on the system.

[36] In conclusion, two-dimensional micromodels provide valuable experimental insight into the relationships among capillary pressure and the phase interfaces within a porous medium. In these systems, mechanical equilibrium is established easily and verified experimentally. The presence of a saturation gradient at each applied pressure is likely a

fundamental aspect of imbibition and drainage for systems in close communication with a reservoir. Future experimental studies need to move into three dimensions to establish whether these results are a consequence of the lowered dimensionality, or are fundamental to systems of any dimensionality.

[37] **Acknowledgments.** The authors wish to acknowledge Rossman Giese for the calculation of interfacial tension values used in this paper. This material is based upon work supported by the National Science Foundation under grant 0509759.

References

- Annable, M. D., J. W. Jawitz, P. S. C. Rao, D. P. Dai, H. Kim, and A. L. Wood (1998), Field evaluation of interfacial and partitioning tracers for characterization of effective NAPL-water contact areas, *Ground Water*, 36(3), 495–503, doi:10.1111/j.1745-6584.1998.tb02821.x.
- Anwar, A. H. M. F., M. Bettahar, and U. Matsubayashi (2000), A method for determining air-water interfacial area in variably saturated porous media, *J. Contam. Hydrol.*, 43, 129–146, doi:10.1016/S0169-7722(99)00103-5.
- Barnes, G. T. and I. R. Gentle (2005), *Interfacial Science*, Oxford Univ. Press, Oxford, U. K.
- Bear, J. (1972), *Dynamics of Fluids in Porous Media*, Dover, Mineola, New York.
- Bear, J. (1979), *Hydraulics of Groundwater*, McGraw-Hill, New York.
- Bear, J. and A. Verruijt (1987), *Modeling Groundwater Flow and Pollution*, D. Reidel, Dordrecht, Netherlands.
- Bradford, S. A., and F. J. Leij (1997), Estimating interfacial areas for multi-fluid soil systems, *J. Contam. Hydrol.*, 27, 83–105, doi:10.1016/S0169-7722(96)00048-4.
- Chen, D. (2006), Experimental investigation of interfacial geometry associated with multiphase flow within a porous medium, Ph.D. thesis, Dep. of Earth and Atmos. Sci., Purdue Univ., West Lafayette, Indiana.
- Chen, L., and T. C. G. Kibbey (2006), Measurement of air-water interfacial area for multiple hysteretic drainage curves in an unsaturated fine sand, *Langmuir*, 22, 6874–6880, doi:10.1021/la053521e.
- Chen, D., L. J. Pyrak-Nolte, J. Griffin, and N. J. Giordano (2007), Measurement of interfacial area per volume for drainage and imbibition, *Water Resour. Res.*, 43, W12504, doi:10.1029/2007WR006021.
- Cheng, J. (2002), Fluid flow in ultra-small structures, Ph.D. thesis, Dep. of Phys., Purdue Univ., West Lafayette, Indiana.
- Cheng, J.-T., L. J. Pyrak-Nolte, D. D. Nolte, and N. J. Giordano (2004), Linking pressure and saturation through interfacial areas in porous media, *Geophys. Res. Lett.*, 31, L08502, doi:10.1029/2003GL019282.
- Collins, R. E. (1961), *Flow of Fluids Through Porous Materials*, Reinhold, New York.
- Colonna, J., F. Brissaud, and J. L. Millet (1972), Evolution of capillary and relative permeability hysteresis, *Soc. Pet. Eng. J.*, 12, 28–38.
- Costanza-Robinson, M. S., and M. L. Brusseau (2002), Air-water interfacial areas in unsaturated soils: Evaluation of interfacial domains, *Water Resour. Res.*, 38(10), 1195, doi:10.1029/2001WR000738.
- Culligan, K. A., D. Wildenschild, B. S. B. Christensen, W. G. Gray, M. L. Rivers, and A. F. B. Tompson (2004), Interfacial area measurements for unsaturated flow through a porous medium, *Water Resour. Res.*, 40, W12413, doi:10.1029/2004WR003278.
- Culligan, K. A., D. Wildenschild, B. S. B. Christensen, W. G. Gray, and M. L. Rivers (2006), Pore-scale characteristics of multiphase flow in porous media: A synchrotron-based CMT comparison of air-water and oil-water experiments, *Adv. Water Resour.*, 29, 227–238, doi:10.1016/j.advwatres.2005.03.021.
- Dalla, E., M. Hilpert, and C. T. Miller (2002), Computation of the interfacial area for two-fluid porous medium systems, *J. Contam. Hydrol.*, 56, 25–48, doi:10.1016/S0169-7722(01)00202-9.
- Deinert, M. R., J.-Y. Parlange, and K. B. Cady (2005), Simplified thermodynamic model for equilibrium capillary pressure in a fractal porous medium, *Phys. Rev. E*, 72, 041203, doi:10.1103/PhysRevE.72.041203.
- Dullien, F. A. L. (1992), *Porous Media: Fluid Transport and Pore Structure*, 2nd ed., Elsevier, New York.
- Giordano, N., and J. T. Cheng (2001), Microfluid mechanics: Progress and opportunities, *J. Phys. Condens. Matter*, 13(15), R271–R295, doi:10.1088/0953-8984/13/15/201.
- Gray, W. G., and S. M. Hassanizadeh (1989), Averaging theorems and averaged equations for transport of interface properties in multiphase systems, *Int. J. Multiphase Flow*, 15(1), 81–95, doi:10.1016/0301-9322(89)90087-6.
- Gray, W. G., and S. M. Hassanizadeh (1991), Unsaturated flow theory including interfacial phenomena, *Water Resour. Res.*, 27(8), 1855–1863, doi:10.1029/91WR01260.
- Gray, W. G., and S. M. Hassanizadeh (1998), Macroscale continuum mechanics for multiphase porous-media flow including phases, interfaces, common lines and common points, *Adv. Water Resour.*, 21, 261–281, doi:10.1016/S0309-1708(96)00063-2.
- Gray, W. G., and C. T. Miller (2006), Thermodynamically constrained averaging theory approach for modeling flow and transport phenomena in porous media systems: 3. Single-fluid-phase flow, *Adv. Water Resour.*, 29, 1745–1765, doi:10.1016/j.advwatres.2006.03.010.
- Gvirtsman, H., and P. V. Roberts (1991), Pore-scale spatial analysis of two immiscible fluids in porous media, *Water Resour. Res.*, 27(6), 1165–1176, doi:10.1029/91WR00303.
- Hassanizadeh, S. M., and W. G. Gray (1990), Mechanics and thermodynamics of multiphase flow in porous-media including interphase boundaries, *Adv. Water Resour.*, 13, 169–186, doi:10.1016/0309-1708(90)90040-B.
- Hassanizadeh, S. M., and W. G. Gray (1993), Thermodynamic basis of capillary pressure in porous media, *Water Resour. Res.*, 29(10), 3389–3405, doi:10.1029/93WR01495.
- Held, R. J., and M. A. Celia (2001), Modeling support of functional relationships between capillary pressure, saturation, interfacial area and common lines, *Adv. Water Resour.*, 24, 325–343, doi:10.1016/S0309-1708(00)00060-9.
- Ioannidis, M. A., I. Chatzis, and A. C. Payatakes (1991), A mercury porosimeter for investigating capillary phenomena and microdisplacement mechanisms in capillary networks, *J. Colloid Interface Sci.*, 143(1), 22–36, doi:10.1016/0021-9797(91)90434-A.
- Kalaydjian, F. A. (1987), A macroscopic description of multiphase flow involving space-time evolution of fluid/fluid interfaces, *Transp. Porous Media*, 2, 537–552.
- Kim, H., P. S. C. Rao, and M. D. Annable (1999a), Consistency of the interfacial tracer technique: Experimental evaluation, *J. Contam. Hydrol.*, 40, 79–94, doi:10.1016/S0169-7722(99)00030-3.
- Kim, H., P. S. C. Rao, and M. D. Annable (1999b), Gaseous tracer technique for estimating air-water interfacial areas and interface mobility, *Soil Sci. Soc. Am. J.*, 63, 1554–1560, 199b.
- Lenhard, R. J. (1992), Measurement and modeling of three-phase saturation-pressure hysteresis, *J. Contam. Hydrol.*, 9, 243–269, doi:10.1016/0169-7722(92)90007-2.
- McClure, J. E., D. Adalsteinsson, C. Pan, W. G. Gray, and C. T. Miller (2006), Approximation of interfacial properties in multiphase porous medium systems, *Adv. Water Resour.*, 30, 354–365, doi:10.1016/j.advwatres.2006.06.010.
- Montemagno, C. D., and W. G. Gray (1995), Photoluminescent volumetric imaging: A technique for the exploration of multiphase flow and transport in porous media, *Geophys. Res. Lett.*, 22(4), 425–428, doi:10.1029/94GL02697.
- Morrow, N. R. (1970), Physics and thermodynamics of capillary action in porous media, in *Flow Through Porous Media*, pp. 104–128, Am. Chem. Soc., Washington, D. C.
- Muccino, J. C., W. G. Gray, and L. A. Ferrand (1998), Toward an improved understanding of multiphase flow in porous media, *Rev. Geophys.*, 36(3), 401–422, doi:10.1029/98RG00878.
- Nolte, D. D., and L. J. Pyrak-Nolte (1991), Stratified continuum percolation—Scaling geometry of hierarchical cascades, *Phys. Rev. A*, 44(10), 6320–6333, doi:10.1103/PhysRevA.44.6320.
- Philip, J. R. (1977), Unitary approach to capillary condensation and adsorption, *J. Chem. Phys.*, 66(11), 5069–5075, doi:10.1063/1.433814.
- Powers, S. E., C. O. Loureiro, L. M. Abriola, and W. J. Weber Jr. (1991), Theoretical study of the significance of nonequilibrium dissolution of nonaqueous phase liquids in subsurface systems, *Water Resour. Res.*, 27(4), 463–477, doi:10.1029/91WR00074.
- Prodanovic, M., W. B. Lindquist, and R. S. Seright (2006), Porous structure and fluid partitioning in polyethylene cores from 3D X-ray microtomographic imaging, *J. Colloid Interface Sci.*, 298, 282–297, doi:10.1016/j.jcis.2005.11.053.
- Pyrak-Nolte, L. J., N. J. Giordano, and D. D. Nolte (2004), Experimental investigation of relative permeability upscaling from the micro-scale to the macro-scale, final report, U.S. Dep. of Energy, Washington, D. C., doi:10.2172/833410.
- Rao, P. S. C., M. D. Annable, and H. Kim (2000), NAPL source zone characterization and remediation technology performance assessment:

- Recent developments and applications of tracer techniques, *J. Contam. Hydrol.*, *45*, 63–78, doi:10.1016/S0169-7722(00)00119-4.
- Rapoport, L. A., and W. J. Leas (1951), Relative permeability to liquid in liquid-gas systems, *Pet. Trans.*, *192*, 83–98.
- Reeves, P. C., and M. A. Celia (1996), A functional relationship between capillary pressure, saturation, and interfacial area as revealed by a pore-scale network model, *Water Resour. Res.*, *32*(8), 2345–2358, doi:10.1029/96WR01105.
- Saripalli, K. P., H. Kim, P. S. C. Rao, and M. D. Annable (1997), Measurement of specific fluid-fluid interfacial areas of immiscible fluids in porous media, *Environ. Sci. Technol.*, *31*(3), 932–936, doi:10.1021/es960652g.
- Schaefer, C. E., D. A. DiCarolo, and M. J. Blunt (2000), Determination of water-oil interfacial area during 3-phase gravity drainage in porous media, *J. Colloid Interface Sci.*, *221*, 308–312, doi:10.1006/jcis.1999.6604.
- Sethian, J. A. (1985), Curvature and the evolution of fronts, *Commun. Math. Phys.*, *101*(4), 487–499, doi:10.1007/BF01210742.
- Shipley (1982), Shipley microelectronic product guide, Newton, Mass.
- Thompson, L. F., C. G. Willson, and M. J. Bowden (1994), *Introduction to Microlithography*, 2nd ed., Am. Chem. Soc., Washington, D. C.
- Topp, G. C. (1969), Soil-water hysteresis measured in a sandy loam and compared with the hysteretic domain model, *Soil Sci. Soc. Am. Proc.*, *33*, 645–651.
- Tuller, M., D. Or, and L. M. Dudley (1999), Adsorption and capillary condensation in porous media: Liquid retention and interfacial configurations in angular porous media, *Water Resour. Res.*, *35*(7), 1949–1964, doi:10.1029/1999WR900098.
- van Genabeek, O., and D. H. Rothman (1996), Macroscopic manifestations of microscopic flows through porous media: Phenomenology from simulation, *Annu. Rev. Earth Planet. Sci.*, *24*, 63–87, doi:10.1146/annurev.earth.24.1.63.
- Wilkinson, D. (1986), Percolation effects in immiscible displacement, *Phys. Rev. A*, *34*(2), 1380–1391, doi:10.1103/PhysRevA.34.1380.

D. Chen, Petroleum Abstracts, University of Tulsa, Tulsa, OK 74104-3189, USA.

N. J. Giordano, D. D. Nolte, and L. J. Pyrak-Nolte, Department of Physics, Purdue University, West Lafayette, IN 47907-2036, USA. (ljpn@physics.purdue.edu)